

Tricolor visible wavelength-selective photodegradable hydrogel biomaterials

Received: 9 September 2022

Teresa L. Rapp  ¹ & Cole A. DeForest  ^{1,2,3,4,5,6} 

Accepted: 10 August 2023

Published online: 29 August 2023

 Check for updates

Photodynamic hydrogel biomaterials have demonstrated great potential for user-triggered therapeutic release, patterned organoid development, and four-dimensional control over advanced cell fates *in vitro*. Current photosensitive materials are constrained by their reliance on high-energy ultraviolet light (<400 nm) that offers poor tissue penetrance and limits access to the broader visible spectrum. Here, we report a family of three photolabile material crosslinkers that respond rapidly and with unique tricolor wavelength-selectivity to low-energy visible light (400–617 nm). We show that when mixed with multifunctional poly(ethylene glycol) macromolecular precursors, ruthenium polypyridyl- and *ortho*-nitrobenzyl (*o*NB)-based crosslinkers yield cyocompatible biomaterials that can undergo spatiotemporally patterned, uniform bulk softening, and multiplexed degradation several centimeters deep through complex tissue. We demonstrate that encapsulated living cells within these photoresponsive gels show high viability and can be successfully recovered from the hydrogels following photodegradation. Moving forward, we anticipate that these advanced material platforms will enable new studies in 3D mechanobiology, controlled drug delivery, and next-generation tissue engineering applications.

Light is a particularly powerful stimulus for gaining spatiotemporal control over dynamic material transformations. In contrast to intrinsic stimuli such as pH, temperature, and protease levels that are challenging to regulate in a biological setting, light's ability to be precisely administered affords unique control over when, where, and to what degree materials undergo pre-programmed responses as well as a route to sidestep challenges associated with patient-to-patient variability in clinical applications. Recognizing this unique utility, the biomaterials community has invested substantial efforts towards the development of photoresponsive hydrogels – water-swollen polymer networks that elicit a prespecified change upon directed light irradiation^{1–4}. The resulting systems have driven significant advances across multiple fields, including cellular biology^{5–10}, drug discovery^{11–15}, tissue engineering platforms for directing cell fate^{16,17}, and organoid culture^{18,19}. Photodynamic hydrogels take advantage of light's

spatiotemporal control to trigger photoinduced material softening^{20,21}, biochemical release^{22–24}, and species uncaging/activation for *in vivo* material modification²⁵.

Despite the early promise of phototunable gels, chemistry- and material-based limitations have precluded the full power of these platforms from being realized². Reliance on organic chromophores to encode photodegradability within hydrogels has historically confined the photocleaving wavelengths to high-energy light – ranging from ≤ 365 nm for *ortho*-nitrobenzyl (*o*NB)-based systems up to 450 nm for some reported photolabile coumarins and bimanes^{26–28}. While some of these chromophores have been highly characterized and are cyocompatible throughout photolysis, the utilization of UV light irradiation has traditionally confined these materials to solely *in vitro* use as high-energy light is poorly penetrant through complex tissue^{3,29}. Additionally, only a limited number of reports have described

¹Department of Chemical Engineering, University of Washington, Seattle, WA 98195, USA. ²Department of Bioengineering, University of Washington, Seattle, WA 98195, USA. ³Department of Chemistry, University of Washington, Seattle, WA 98195, USA. ⁴Institute of Stem Cell & Regenerative Medicine, University of Washington, Seattle, WA 98109, USA. ⁵Molecular Engineering & Sciences Institute, University of Washington, Seattle, WA 98195, USA. ⁶Institute for Protein Design, University of Washington, Seattle, WA 98195, USA.  e-mail: procole@uw.edu

materials that are sensitive to multiple orthogonal wavelengths, of which nearly all crosslinkers employed rely heavily on near- and far-UV light^{27,28,30-33}, thereby missing significant opportunities for cyto-compatible material multiplexing by taking advantage of the entire spectrum of visible and IR light. A collection of photocleavable crosslinkers that distinctly responds to an expanded portion of electromagnetic spectrum, enabling deeper tissue penetration and multiplexed wavelength-selective material modulation using differently colored light, would enable exciting new directions for phototunable hydrogel platforms.

Seeking to expand light response into the visible range, we turned our attention towards ruthenium (Ru) polypyridyl complexes, which continue to gain new and unique ground in the world of photochemistry^{34,35}. These compounds are highly photoactive and undergo covalent bond breakage upon visible light irradiation, with quantum yields of photodissociation many times greater than current organic chromophores and reaching 0.1–0.6 in many cases^{30,36,37}. Capitalizing on these advances, Ru complexes have found utility in the biochemical space as photocaging groups^{35,38,39} and in the generation of photoresponsive micelles for drug delivery⁴⁰. Though most ruthenium compounds bearing 2,2'-bipyridine ligands commonly absorb blue light (420–450 nm), comparatively simple syntheses can yield species with shifted

absorbances extending into the red and near-IR^{41,42}. With their radical-free ligand exchange³⁹, engineered cytocompatibility, and high photoefficiency, we postulated that uniquely visible light-responsive biomaterials could be created through direct inclusion of such Ru complexes in a polymer backbone, providing a route to next-generation photodynamic hydrogels.

In this work, we describe the synthesis and properties of a unique series of photolabile crosslinkers, including two based on ruthenium compounds: (1) Ru(2,2'-biquinoline)₂(4-azidobutanenitrile)₂ (denoted Rubiq); (2) (Ru(2,2'-bipyridine)₂(4-azidobutanenitrile)₂ (Rubpy); and (3) an established *o*NB⁴³ with wavelength-separated λ_{max} capable of respectively responding selectively to three different colors of visible light – red (617 nm), green (530 nm), and blue (405 nm) (Fig. 1a, b). Mixing four-arm poly(ethylene glycol) (PEG) end-functionalized with bicyclononyne (PEG-tetraBCN) together with the bis(azide)-modified photolinkers with 1:1 stoichiometry with respect to their reactive groups, idealized step-growth polymeric gels can be readily formed through bioorthogonal strain-promoted azide-alkyne cycloaddition (SPAAC) (Fig. 1c)⁴⁴. Taking advantage of crosslinkers designed to rapidly photolyze in a cytocompatible and visible wavelength-selective manner, we anticipated being able to achieve multiplexed material degradation in the presence of living cells and through complex tissue.

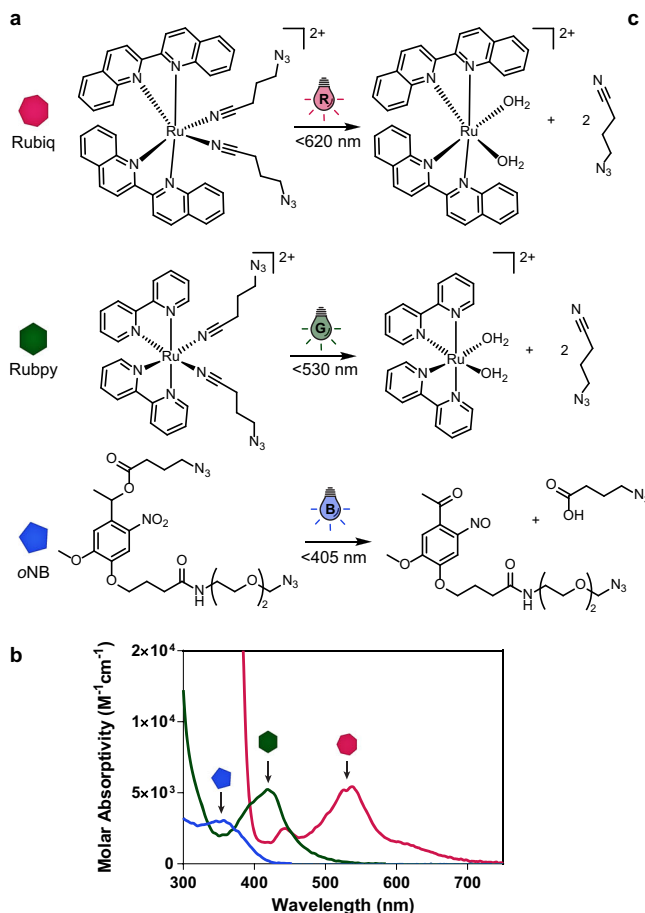


Fig. 1 | Photodegradable crosslinkers cleave in a visible wavelength-selective manner. **a** A novel crosslinkers Rubiq (pink heptagon), Rubpy (green hexagon), and *o*NB (blue pentagon) undergo photolysis. Upon absorption of a photon, each ruthenium complex undergoes ligand exchange via population of a triplet metal-centered state via intersystem crossing from the low-lying metal-to-ligand charge transfer (MLCT) band, resulting in heterolytic ligand/solvent exchange. Crosslinkers are modified with two azides for direct incorporation into hydrogel

networks. **b** Absorbance spectra of Rubiq, Rubpy, and *o*NB. Each crosslinker exhibits an extended absorbance spectrum beyond their λ_{max} permitting excitation at wavelengths lower than λ_{max} . **c** PEG-based hydrogel formation occurs spontaneously upon mixing each crosslinker with 4-arm PEG-BCN via strain-promoted azide-alkyne cycloaddition. Resulting hydrogels degrade under red, green, or blue light with perfect unidirectional orthogonality (>617 nm for Rubiq, >530 nm for Rubpy, and >405 nm for *o*NB).

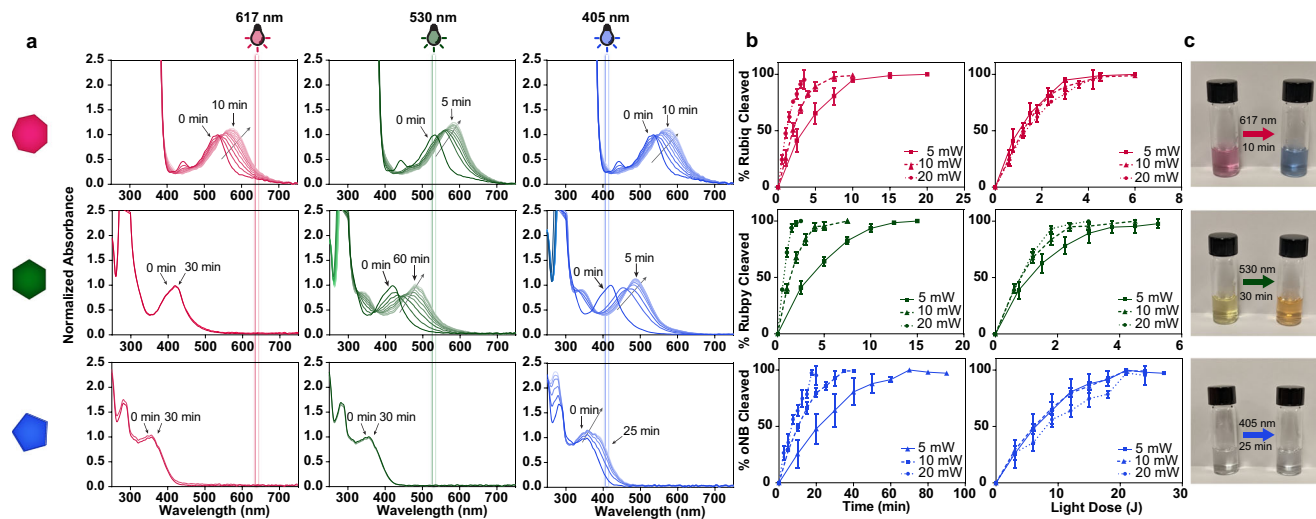


Fig. 2 | Photolabile crosslinkers can be selectively cleaved with differently colored visible light. **a** Rubiq (pink heptagon), Rubpy (green hexagon), and oNB (blue pentagon) individually subjected to 617, 530, and 405 nm light (10 mW cm^{-2} , 0–60 min) undergo wavelength-selective photolysis, indicated by absorbance spectral changes. **b** Photolysis proceeds efficiently with varied power (5, 10, 20 mW)

in a light dose-dependent manner. Here, light dosage is calculated as the product of light intensity and exposure time. $n = 3$ for each photolysis, error bars represent standard deviation about the experimental mean. **c** Color change was observed for Rubiq and Rubpy upon irradiation (10 mW, varied wavelengths and exposure times) due to the significant absorbance shift following ligand exchange.

Results

Synthesis and photochemical characterization of Rubiq, Rubpy, and oNB-based crosslinkers

Photolabile crosslinkers were each synthesized with flanking azides, permitting their incorporation into bulk hydrogels via SPAAC. Rubiq and Rubpy were respectively synthesized in a two- and one-step processes from $\text{Ru}(\text{bpy})_2\text{Cl}_2$ or RuCl_3 and 2,2'-biquinoline, whereby azide-bearing ligands (4-azidobutanenitrile) were coordinated to form symmetrical Ru-based crosslinkers. The bis(azide) oNB was synthesized following published protocol with minimal changes⁴³ (see Methods for synthetic details). All crosslinkers were synthesized, purified, and characterized by ^1H NMR and electrospray ionization mass spectroscopy (ESI-MS, Supplementary Method 1, Supplementary Figs. 1–6) with appreciable overall yields (Rubiq, 27%; Rubpy, 77%; oNB, 17%).

Upon irradiation with the appropriate wavelengths of light, Rubiq and Rubpy undergo ligand exchange with a solvent molecule (in this case, water) due to population of a metal-centered antibonding orbital (Fig. 1a, Supplementary Fig. 7). Rubiq and Rubpy exhibit low-energy absorbance bands due to low-lying metal-to-ligand charge transfer (MLCT) states common in ruthenium polypyridyl complexes⁴⁵. As expected, the extended pi bond structure of 2,2'-biquinoline gave a bathochromic shift in peak absorbance of Rubiq to a λ_{max} of 535 nm, significantly red shifted when compared with the 2,2'-bipyridine-containing Rubpy compound and oNB⁴⁶. All crosslinkers exhibited a significant λ_{max} with a slow decay in absorptivity extending well into the visible range, permitting off-peak photon absorbance and population of antibonding orbitals at low energies (Fig. 2a). For this study, Rubiq was photocleaved using 617 nm ($\epsilon = 43 \text{ M}^{-1}\text{cm}^{-1}$), Rubpy with 530 nm ($\epsilon = 14 \text{ M}^{-1}\text{cm}^{-1}$), and oNB at 405 nm ($\epsilon = 118 \text{ M}^{-1}\text{cm}^{-1}$), wavelengths commonly accessible through inexpensive LED light sources that balanced photocleavage efficiency and spectral separation.

To probe the mechanism of photomediated ligand exchange in the Ru crosslinkers, Rubiq and Rubpy (5 mM) were analysed by ^1H NMR and ESI-MS over 60 min of exposure (10 mW cm^{-2} , 617 nm and 7.8 mW cm^{-2} , 530 nm respectively). ^1H NMR revealed exchange of both

azide-bearing ligands within the first 2.5 minutes of light exposure, Supplementary Figs. 8, 9). This trend was further confirmed through ESI-MS analysis, which additionally indicated that 2,2'-biquinoline and 2,2'-bipyridine ligands remain attached to Ru as expected (Supplementary Figs. 10, 11). Motivated by an interest to use these in the presence of living cells, we further analysed whether singlet oxygen ($^1\text{O}_2$) generation would accompany crosslinker photolysis, as it does when similar compound $\text{Ru}(\text{bpy})_3$ is exposed to light^{47,48}. While $^1\text{O}_2$ was detected for all linkers, each yielded statistically significantly less $^1\text{O}_2$ than $\text{Ru}(\text{bpy})_3$ under matched illumination conditions, with Rubpy producing less than Rubiq and oNB (Supplementary Fig. 12). Since *ortho*-nitrobenzyl-based crosslinkers have been extensively demonstrated as cytocompatible and $\text{Ru}(\text{bpy})_3$ is regularly exploited as a visible light-mediated photoinitiator for cell encapsulation, these results were encouraging.

This series of crosslinkers was shown to be unidirectionally orthogonal: red light (617 nm) irradiation led to photolysis of Rubiq only, green light (530 nm) irradiation photolyzed both Rubiq and Rubpy but left oNB intact, and blue light (405 nm) photolyzed all three crosslinkers (Fig. 2a). This is demonstrated by the presence or absence of a shift in absorbance spectrum upon irradiation; all three compounds undergo a change in their electronic structure upon photolysis which is reflected in the absorbance spectra. The insensitivity of Rubpy to high doses of red light, as well as oNB to extended exposure to red and green light, demonstrates wavelength selectivity of the small molecule crosslinkers *in situ*.

The appearance of a new absorbance maximum of photoproducts was used to determine the quantum yield (QY) of photocleavage at the wavelengths used in this study (Fig. 2b, Table 1). Light at 617 nm, 530 nm, and 405 nm at 5, 10, and 20 mW were used for the QY determination. As expected, faster photocleavage for each compound accompanied higher light intensities. When extent of photolysis was normalized to total light dosage (i.e., the product of intensity and exposure time), cleavage traces collapsed onto a single curve for each species (Fig. 2b). Rubpy has the highest QY of the three (0.29 ± 0.04), consistent with prior reports for $\text{Ru}(\text{bpy})_2\text{L}_2$ complexes under visible

Table 1 | Photokinetic constants

Compound	λ_{max} (nm)	$\lambda_{\text{excitation}}$ (nm)	Quantum Yield (Φ_{pr})	Molar Absorptivity (ϵ , $\text{M}^{-1}\text{cm}^{-1}$)	Efficiency ($\Phi \cdot \epsilon$)
Rubiq	535	617	0.016 ± 0.009	43	0.688
Rubpy	420	530	0.29 ± 0.04	14	4.06
<i>o</i> NB	365	405	0.004 ± 0.003	118	0.472

light irradiation^{30,37,49}. Rubiq's QY (0.016 ± 0.009) was found to be lower than that of Rubpy, due to the bathochromic shift decreasing intersystem crossover efficiency into the metal-centered antibonding orbital⁴⁶. Though *o*NB has a very low QY at 405 nm (0.004 ± 0.003), its higher molar absorptivity enables photocleavage under visible irradiation with reasonable efficiency. Photolysis was found to be complete for all three crosslinkers within 30 minutes at 10 mW (Fig. 2b). Significant color change accompanied photolysis for each compound, particularly for Rubiq, providing a useful handle for qualitative crosslinker cleavage determination in hydrogel formulations (Fig. 2c).

Multiplexed hydrogel degradation via visible light irradiation
Having demonstrated the wavelength orthogonality and high efficiency of this series of photocleavable molecules, we sought to employ them as crosslinkers in PEG-based hydrogel systems. To create visible light-degradable hydrogels, Rubiq, Rubpy, and *o*NB were polymerized with PEG-tetraBCN via SPAAC chemistry (Fig. 3a). Though gelation kinetics varied slightly with crosslinker identity, each formulation resulted in equivalently stiff hydrogels ($G' \sim 2.5$ kPa), as quantified using *in situ* rheometry (Fig. 3b). Following complete gelation, hydrogels crosslinked with Rubiq, Rubpy, and *o*NB were individually subjected to sequential treatments (35 min each) of 617 nm, 530 nm, and 405 nm light (10 mW cm^{-2}), with photodegradation assessed rheometrically. Rubiq-based gels degraded rapidly upon red-light illumination, while those containing Rubpy and *o*NB persisted; Rubpy subsequently degraded with green light with *o*NB materials unchanged; finally, blue light afforded rapid cleavage of the remaining *o*NB-crosslinked hydrogel (Fig. 3c). Hydrogel stability was dependent on temperature: when stored in the dark, Rubiq-crosslinked hydrogels were stable (defined as $<30\%$ degradation, wherein hydrogels swelled but maintained their original shape and structural integrity) at room temperature for 24 h, but were fully dissolved by this timepoint when stored at 37 °C; Rubpy hydrogels were stable for 7 days at room temperature, but only 48 h at 37 °C; *o*NB-crosslinked hydrogels are considered completely stable, experiencing no loss in material integrity over the course of the experiment at both temperatures (Supplementary Fig. 13). Results highlight that the gels can be photodegraded in a visible wavelength-selective manner as designed.

To access intermediate bulk hydrogel stiffnesses, hydrogels were cast with equal amounts of the photolabile crosslinkers (i.e., 1:1:1 Rubiq:Rubpy:*o*NB) alongside varied percentages (0–90%) of photo-stable diazido-tri(ethylene glycol) crosslinker (denoted TEG), while keeping the total crosslinker concentration constant (Fig. 3d, Supplementary Fig. 14). When sequentially subjected to red, green, and blue light (10 mW cm^{-2} , 35 min each) and analyzed rheometrically, hydrogels partially softened to intermediate moduli or fully degraded in a manner dependent on crosslinker makeup and wavelength-selectivity. Consistent with polymer network rubber elasticity theory, the incorporation of stable TEG crosslinks into the matrix at varying percentages stabilized the hydrogel at intermediate stiffness following complete lysis of photocleavable crosslinks. Hydrogels with low percentages of TEG (10%) lost all elastic properties after exposure to red + green light. When TEG comprised $>60\%$ of crosslinks, the hydrogel was no longer fully photodegradable, yielding a soft stable hydrogel following complete light treatment (Fig. 3e).

To illustrate that wavelength-selectivity could be used to dynamically pattern hydrogel multimatials, we formulated multilayered hydrogels composed of distinctly patterned regions of Rubiq, Rubpy, and *o*NB using open-microfluidic additive manufacturing methods⁵⁰. These multifunctional hydrogels were sequentially exposed to red, green, and blue light, and imaged using digital photography (Fig. 3f). Following red-light illumination, Rubiq exhibited the pink-to-purple color change observed previously to accompany degradation, while Rubpy and *o*NB were visibly unaltered. Treatment with green light caused Rubpy to lose its yellow color and degrade, leaving only *o*NB regions intact. Final treatment with blue light yielded complete material dissolution.

Encouraged by the hydrogel's rapid response to low-energy visible light, we next sought to examine whether hydrogels could be degraded through complex tissue. Skin-on pork belly was dissected and hydrogels placed at varying depths; a Rubiq-crosslinked hydrogel was deposited 2 cm below the skin surface, a Rubpy hydrogel at 1 cm, and *o*NB (modified with Cy5-azide to enhance visualization) at 0.5 cm. Gels were respectively subjected to red, green, and blue light (50 mW cm^{-2} at the skin) and *in-tissue* degradation was visually monitored (Fig. 3h). Hydrogel dissolution was observed for all three hydrogels following <2 h illumination at the depths reported, mirroring previously reported studies with Ru-based photocages⁵¹. To the best of our knowledge, this is the first time that a photodegradable biomaterial has been directly controlled at these tissue depths, highlighting the potential of these materials for future *in vivo* applications.

Cell viability throughout encapsulation and release from tricolor-responsive hydrogels

Having demonstrated that hydrogel responses could be controlled in a wavelength-specific manner using visible light, we next sought to investigate the cytocompatibility of these crosslinkers in solution, as well as during gel formation and subsequent photodegradation. Human bone marrow-derived stromal cells (hSSs) and mouse 10T1/2 immortalized fibroblasts were exposed to Rubiq and Rubpy (1 mM) for 3 h prior to proliferation assessment via longitudinal viability assay (RealTime Glo, Promega, Supplementary Figs. 15, 16). Rubiq exposure led to significant loss in viability as well as an arrest of the cell cycle for both cell types. Rubpy exhibited no toxicity for hSSs, and only modest decrease in early 10T1/2 proliferation rates. To probe the mechanism of cell death, we measured caspase 3 activity levels as a measure of apoptosis 24 h following crosslinker exposure and found no significant differences, suggesting an alternative mechanism (Supplementary Figs. 17, 18). Interestingly, pre-reacting both Rubiq and Rubpy with a stoichiometric excess of mono-functionalized methoxy-PEG-BCN yielded di-PEGylated species that was markedly less toxic than the free crosslinkers. These results suggest that crosslinker toxicity is greatly reduced upon polymerization into a PEG-based hydrogel network (Supplementary Figs. 15, 16).

To determine cell survival throughout encapsulation in a hydrogel, hSSs, human mesenchymal stem cells (hMSCs), and 10T1/2 cells were encapsulated (5×10^6 cells mL^{-1}) in Rubiq, Rubpy, and *o*NB-crosslinked hydrogels (Fig. 4a, Supplementary Figs. 19, 20). Live/dead staining with calcein/ethidium homodimer and fluorescent confocal imaging was performed 24 h after encapsulation. Reasonably high viability (between 40–95%) was observed in all cases (Fig. 4b, c), consistent with SPAAC's reported biocompatibility for gel formation and that of the crosslinkers⁵², though some cell- and crosslinker-type dependencies were observed.

Photorelease from hydrogels had a significant effect on viability, with results again varying across the three different cell types. To assess the cytocompatibility of photodegradation, cell-laden hydrogels were photodegraded with red, green, or blue visible light 1 day post encapsulation. In a subset of the gels, released cells were left

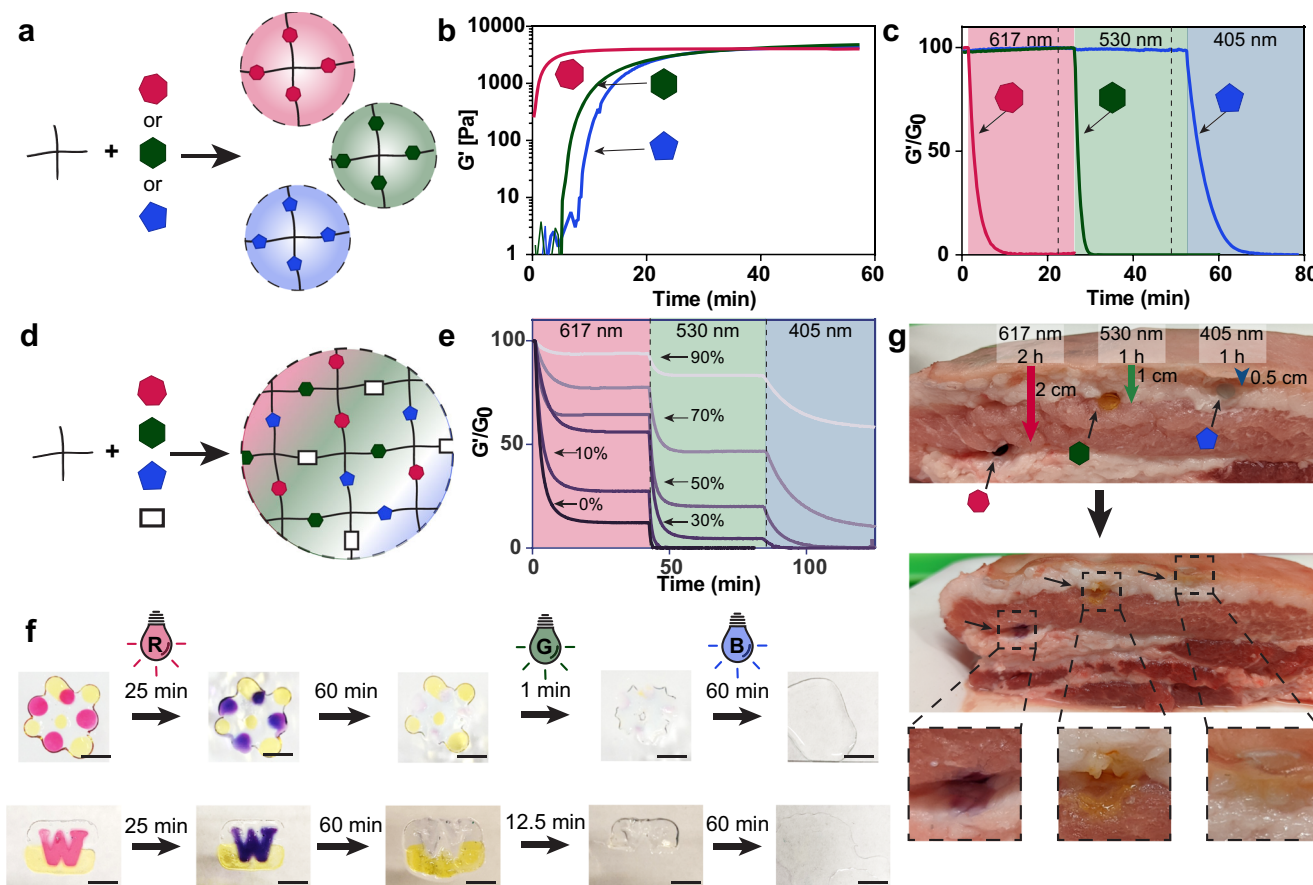


Fig. 3 | Wavelength-orthogonal hydrogel degradation via red, green, and blue light. **a** Hydrogels formed via SPAAC chemistry between PEG-tetraBCN and the azide-flanked crosslinkers. **b** Rubiq (pink heptagon)-, Rubpy (green hexagon)-, and oNB (blue pentagon)-crosslinked hydrogels form equivalently stiff hydrogels ($G' \sim 2-3$ kPa) as determined rheometrically. **c** Individually crosslinked hydrogels are unidirectionally orthogonally degraded, with stable storage modulus observed in Rubpy-crosslinked gels under red light irradiation and oNB-crosslinked gels under red and green light irradiation. **d** Hydrogels were formed with equal ratios of all three photolabile crosslinkers and increasing amounts of nondegradable diazidotri(ethylene glycol) (TEG) crosslinker (0–90%, white rectangle). **e** Intermediate stiffnesses were accessible through partial degradation of hydrogel crosslinks.

Hydrogels were exposed to red, green, then blue light (35 min each, 10 mW cm^{-2}) to selectively cleave specific amounts of crosslinks within the material. Reported percentages refer to the amount of stable, non-cleavable crosslink present in the material. **f** Spatial control over hydrogel degradation demonstrated by the casting of individually crosslinked hydrogels in close proximity. Open microfluidic methodologies were used to cast interconnected multimaterial geometries; exposure to red light resulted in the center Rubiq degradation, observed after a 60-min wash. Subsequent exposures to green and blue light rapidly degraded the Rubpy and oNB portions, respectively. Scale bar = 5 mm. **g** Rubiq hydrogels were completely degraded through up to 2 cm of complex tissue (skin-on pork belly shown here), Rubpy hydrogels through 1 cm, and oNB (dyed with Cy5) through 0.5 cm.

suspended in hydrogel photoproducts for an additional 24 h, after which the cells that adhered were stained for viability (Fig. 4c). Fibroblasts showed normal morphology 24 h after plating, suggesting the photodegradation process did not alter them significantly. To confirm viability following release, cells were collected following hydrogel degradation and assessed directly for viability via flow cytometry (Fig. 4d, Supplementary Fig. 21). Though viability was generally high, results demonstrated that fibroblasts released from Rubiq-crosslinked gels exhibited a significant loss in viability of approximately 40%, suggesting that the Rubiq photoproduct may be partially cytotoxic. Proliferation rates of gel-released hSSs and hMSCs were also assessed via EdU (5-ethynyl-2'-deoxyuridine) staining and quantification of newly synthesized DNA; while hMSC cells showed minimal EdU⁺ nuclei, hSSs showed significant recovery of proliferative behaviour following photorelease, but again with poorer performance in the Rubiq-crosslinked systems (Supplementary Figs. 19, 20). Prior studies on this type of compound suggests the extended aromatic ligands on Ru compounds contribute to their instability and enhanced cytotoxicity⁵³, though future designs may include incorporation of hydrophilic groups to decrease cellular uptake leading to their toxicity⁴².

Taking advantage of the spatial resolution afforded by this hydrogel system using orthogonal wavelengths of light, unique cell populations were encapsulated and recovered from individual hydrogels. hSSs stably expressing either mCherry, GFP, or BFP were encapsulated in Rubiq, Rubpy, and oNB-crosslinked hydrogels, respectively (Fig. 4e). Upon irradiation with red, green, or blue light, selective hydrogel degradation was observed by confocal microscopy (Fig. 4f). Following degradation, the gel-liberated cell populations were collected and analyzed via flow cytometry. Harvested cell collections matched the expected color composition: 617 nm light released only mCherry⁺ cells, 530 nm yielded matched populations of mCherry⁺ and GFP⁺, and 405 nm light degraded all three hydrogels and gave equivalent counts of mCherry⁺, GFP⁺, and BFP⁺ cells (Fig. 4g, Supplementary Fig. 22). Results further demonstrate wavelength orthogonality and multiplexability of cell release from tricolor visible light-responsive gels.

Discussion

In summary, photolabile crosslinkers Rubiq, Rubpy, and oNB provide a route towards the first tricolor visible light-degradable gel system. We have established that these crosslinkers are synthetically accessible

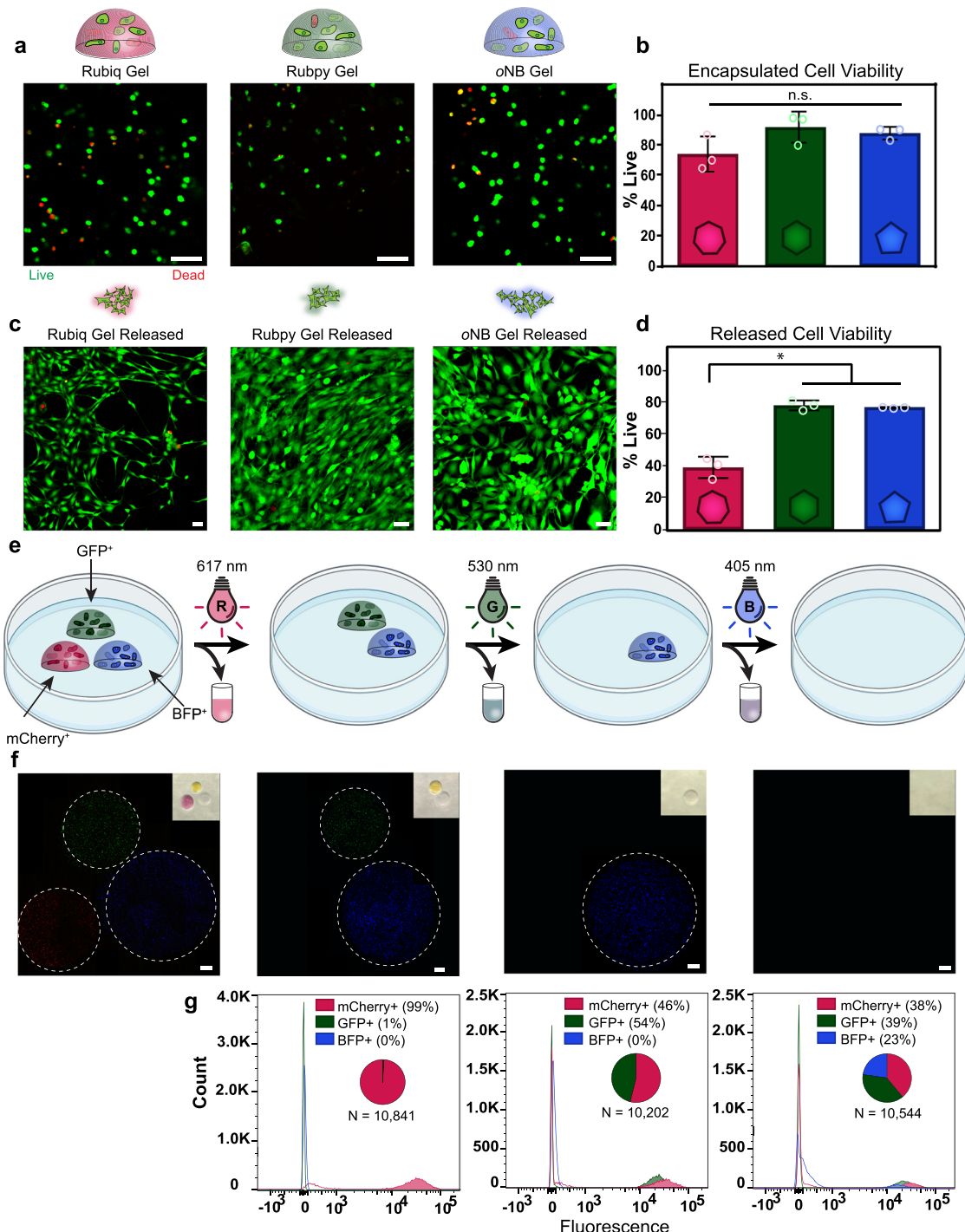


Fig. 4 | Cell viability following encapsulation in and photorelease from Rubiq, Rubpy, and oNB-crosslinked hydrogels. **a** Live/dead staining of 10T1/2 fibroblasts encapsulated in individually crosslinked hydrogels, shown as single z-slice obtained via confocal micrography. Calcein (green) and ethidium homodimer (EtHD, red) dyes were used for live and dead staining respectively. Scale bar = 50 μ m.

b Encapsulated cell viability at 24 h post encapsulation (cell counts collected from 40 μ m \times 1 mm \times 1 mm section through the vertical center of the hydrogel). Cell counting revealed no statistical difference ($p > 0.05$, one-way ANOVA) in cell viability across all crosslinkers at 24 h. $n = 3$ individual biological replicates, error bars represent standard deviation about the experimental mean. **c** Rubiq, Rubpy, and oNB hydrogels were exposed to red, green, or blue light respectively (617 nm, 530 nm, 405 nm; 10 mW cm^{-2}) and the released fibroblasts allowed to settle to the bottom of the well over 24 h prior to imaging. Surviving cells exhibited classical

fibroblast morphology upon calcein green/EtHD staining. Scale bars = 50 μ m.

d High levels of viable cells were recovered from each hydrogel formulation, though cells released from Rubiq hydrogels showed lower levels of viability compared to Rubpy and oNB. $^*p = 0.0036$ by one-way ANOVA, $n = 3$ individual biological replicates, error bars represent standard deviation about the experimental mean. **e** mCherry⁺, GFP⁺, and BFP⁺ hSS cells were encapsulated in Rubiq, Rubpy, and oNB hydrogels respectively. 24 h after encapsulation, hydrogels were exposed to 617 nm, 530 nm, or 405 nm light. **f** Images of hydrogels bearing mCherry⁺, GFP⁺, or BFP⁺ hSS cells following light exposure. Scale bars = 500 μ m. Experiment performed in biological triplicate with similar results; representative images given. **g** Flow cytometry histograms show only expected cell populations were released into the media, demonstrating the orthogonality of the hydrogel system.

with moderate yields and photoresponsive to low-energy light. These species are highly photoactive under visible light irradiation permit facile synthesis of PEG-based hydrogels that rapidly and orthogonally degrade under red (617 nm), green (530 nm) and blue (405 nm) light. The use of low-energy light permits hydrogel degradation through complex tissue up to 2 cm in depth, while wavelength-orthogonality enables sequential and spatial control over hydrogel degradation. We have demonstrated crosslinker cytocompatibility, with moderate-to-high viability observed for three distinct cell types upon hydrogel encapsulation and 3D culture. Exploiting their wavelength-selective degradation, we demonstrated multiplexed cell populations recovery, a feature that is likely to be useful for *in vivo* cell delivery applications. Moving forward, we anticipate that these materials will prove enabling for additional applications in mechanobiology, 4D cell culture, and controlled therapeutic release.

Methods

General synthetic methods

All reactions and purification protocols were performed under red light. All solvents and chemicals were used as received with no further purification. All reagents and solvents were obtained from Fisher Scientific unless otherwise stated and used without further purification.

4-azidobutynitrile. 4-bromobutynitrile (1 mL, 10 mmol) and sodium azide (1.3 g, 20 mmol) were dissolved in dimethylsulfoxide (DMSO, 15 mL) and stirred overnight at 55 °C. The reaction was cooled to room temperature, diluted with water to 50 mL, extracted with diethyl ether (3 × 50 mL), dried over Na₂SO₄, and the ether was removed under vacuum to give the product as a light-yellow oil. SAFETY HAZARD: 4-azidobutynitrile is isolated with DMSO in the final form. It should never be fully dried, as it is an explosive small molecule azide when concentrated. Yield: 1.017 g, 92%. ¹H NMR: (CDCl₃, 300 MHz) δ 3.50 (t, 2H, *J*=6.34), 2.48 (t, 2H, *J*=7.05), 1.92 (quint, 2H, *J*=12.96).

Ru(biquinoline)₂Cl₂ (Ru(biq)₂Cl₂). RuCl₃ (anhydrous, 99.96% trace metal basis, 400 mg, 1.93 mmol), hydroquinone (444 mg, 4 mmol), and LiCl (480 mg, 11.3 mmol) were suspended in dimethylformamide (DMF, 10 mL) and bubbled with N₂ for 15 min. 2,2'-biquinoline (1 g, 4 mmol) was added, and the reaction was heated to 130 °C for 1 h until color appeared forest green, then cooled to room temperature. Reaction was added dropwise to 800 mL deionized water and filtered to collect a dark green-black solid. Solid was dissolved in dichloromethane (200 mL), solvent was reduced to 100 mL under vacuum, then added to diethyl ether (400 mL) and filtered to collect Ru(biq)₂Cl₂ as a dark green solid. Product was used without further purification. Yield: 805 mg, 61%.

Ru(biq)₂(4-azidobutynitrile)₂[Cl₂] (Rubiq). Ru(biq)₂Cl₂ (250 mg, 0.365 mmol) and silver hexafluorophosphate (275 mg, 1.08 mmol) were dissolved in methanol (40 mL, stored over molecular sieves) and stirred at 55 °C in the dark until reaction turned blue and white silver chloride powder was observed (15 min). 4-azidobutynitrile (100 μL, 0.945 mmol) was added, and the reaction stirred at 55 °C for 1 h until color turned pink. Reaction was cooled to room temperature, filtered to remove silver chloride, and methanol was removed by rotary evaporation. Ru(biq)₂(4-azidobutynitrile)₂ was purified by silica flash chromatography with 1:4 acetonitrile:dichloromethane as the eluent.

Ru(biq)₂(4-azidobutynitrile)₂[PF₆]₂ was converted to the chloride salt by anion-exchange resin. RuPink[PF₆]₂ was passed over Amberlite IRA-410 (Cl Form) resin using methanol as the eluent, giving Ru(biq)₂(4-azidobutynitrile)₂[Cl]₂ as the water-soluble form (denoted Rubiq). Yield: 159 mg, 48%. Overall yield: 27%. ¹H NMR: (CD₃CN, 300 MHz) δ 9.14 (broad s, 2H), 8.68 (d, 2H, *J*=8.69), 8.36 (d, 2H, *J*=7.99), 8.31 (d, 2H, *J*=8.09), 8.21 (broad s, 2H), 8.02 (t, 2H, *J*=7.27),

7.91 (d, 2H, *J*=7.84), 7.50 (t, 2H, *J*=7.04), 6.87 (t, 2H, *J*=7.17), 6.75 (d, 2H, *J*=8.4), 3.08 (t, 4H, *J*=6.42), 2.75 (t, 4H, *J*=7.25), 1.65 (quint, 4H, *J*=6.57). Expected mass [H⁺, m/2]: 417.11, observed mass: 417.1125 (m/2).

Ru(bpy)₂(4-azidobutynitrile)₂[Cl₂] (Rubpy).

Ru(bipyridine)₂Cl₂·2H₂O (200 mg, 0.38 mmol) and silver hexafluorophosphate (212 mg, 0.83 mmol) were dissolved in methanol (stored over molecular sieves, 40 mL) and stirred at 55 °C for 15 min. 4-azidobutynitrile (390 μL, 3.7 mmol) was added and the reaction stirred at 55 °C for 2 h until color changed from red to orange. Reaction mixture was cooled to room temperature and filtered to remove silver chloride, then concentrated by rotary evaporation. The product (denoted Rubpy) was purified by silica flash chromatography with 4:1 dichloromethane:acetonitrile as the eluent, collecting the major yellow band. Yield: 22 mg, 84%. Overall yield: 77%. ¹H NMR: (CD₃CN, 300 MHz) δ 9.61 (d, 2H, *J*=4.95), 8.83 (d, 2H, *J*=8.07), 8.69 (d, 2H, *J*=8.10), 8.43 (t, 2H, *J*=7.16), 8.12 (t, 2H, *J*=7.16), 8.00 (t, 2H, *J*=6.00), 7.93 (d, 2H, *J*=5.70), 7.46 (t, 2H, *J*=6.00), 3.37 (t, 4H, *J*=6.33), 3.00 (t, 4H, *J*=6.74), 1.90 (quint, 4H, *J*=6.58). Expected mass [H⁺, m/2]: 317.08, observed mass: 317.08 (m/2).

4-azidobutanoic acid (N₃-COOH). N₃-COOH was synthesized based on published procedures and used with minor modifications⁴³. Ethyl-4-bromobutyrate (36.6 mL, 254 mmol) and sodium azide (25 g, 380 mmol) were dissolved in DMSO (375 mL) and reacted at 55 °C overnight. The reaction was cooled to room temperature and diluted with water (250 mL) and extracted with diethyl ether (3 × 100 mL). The organic layer was washed with brine (250 mL) and dried over Na₂SO₄, and concentrated by rotary evaporator to give the intermediate ethyl-4-azidobutanoate as a yellow oil. Yield: 32.5 g, 80%.

Ethyl-4-azidobutanoate (32.5 g, 0.205 mmol) was dissolved in 150 mL of methanol. 1M sodium hydroxide (aqueous, 250 mL) was added and the mixture was stirred at room temperature for 3 h. Methanol (~75 mL) was partially removed by rotary evaporation and concentrated hydrochloric acid (HCl) was added until the pH reached 1. The product was extracted into diethyl ether (3 × 250 mL), dried over Na₂SO₄, and the ether was removed to give 4-azidobutanoic acid as a yellow oil. Yield: 27 g, 84%. ¹H NMR (CDCl₃, 300 MHz) 6.29 (br s, 1H), 3.51 (q, 2H, *J*=7.04), 3.37 (t, 2H, *J*=6.72), 2.45 (quint, 2H, *J*=7.23), 1.21 (t, 2H, *J*=7.03).

4-(4-(4-azidobutanoyl)oxyethyl)-2-methoxy-5-nitrophenoxy butanoic acid (N₃-oNB-COOH). N₃-COOH (27 g, 209 mmol) and N,N'-Dicyclohexylcarbodiimide (DCC, 13.8 g, 67 mmol) were mixed under nitrogen in a flame-dried flask. Dry dichloromethane (DCM, 170 mL) was added and the reaction stirred at room temperature for 1 h. Solid urea byproduct was filtered over glass frit and the reaction mixture concentrated by rotary evaporation (filtration step repeated if more byproduct precipitate was observed).

HO-oNB-COOH (4-(4-(1-hydroxyethyl)-2-methoxy-5-nitrophenoxy)butanoic acid, 4.2 g, 14 mmol) and 4-dimethylaminopyridine (DMAP, 86 mg, 0.7 mmol) were mixed with the crude anhydride and dissolved in minimal dichloromethane (DCM, 100 mL). Pyridine (1.13 mL, 14 mmol) was added and reaction was stirred under nitrogen overnight until color turned dark brown. Reaction was washed with saturated sodium bicarbonate (NaHCO₃, 250 mL) and 1M aqueous HCl and concentrated by rotary evaporation. Reaction was dissolved in 1:1 water:acetone (500 mL) and stirred overnight at room temperature. SAFETY HAZARD: washes with 1M HCl will generate CO₂ gas; vent appropriately.

Acetone was removed by rotary evaporation and product extracted into dichloromethane (3 × 250 mL). The organic layer was washed with 1M HCl, dried over sodium sulfate and concentrated. Product was purified by flash silica column chromatography, 20–40%

ethyl acetate in hexanes with 1% acetic acid, product eluted as trailing yellow band giving *N*₃-*o*NB-COOH as a yellow oil. Yield: 4.3 g, 71%. ¹H NMR (CDCl₃, 300 MHz) δ 7.57 (s, 1H), 7.10 (s, 1H), 6.21 (q, 1H, *J* = 6.44), 4.08 (t, 2H, *J* = 6.47), 3.96 (s, 3H), 3.32 (t, 2H, *J* = 6.84), 2.43 (t, 2H, *J* = 6.21), 2.38 (t, 2H, *J* = 6.34), 1.96 (quint, 2H, *J* = 6.91), 1.76 (t, 2H, *J* = 6.98), 1.58 (d, 3H, *J* = 6.54).

1-(4-((2-(2-azidoethoxy)ethoxyethyl)amino)-4-oxobutoxy)-5-methoxy-2-nitrophenyl)ethyl 4-azidobutanoate (*o*NB). *N*₃-*o*NB-COOH (2.1 g, 5 mmol), 1-[Bis(dimethylamino)methylene]-1H-1,2,3-triazolo[4,5-*b*]pyridinium 3-oxid hexafluorophosphate (HATU, 950 mg, 2.5 mmol, Sigma Aldrich), and diisopropylamine (DIEA, 3.56 mL, 20 mmol, Chem-Impex International) were dissolved in DMF and stirred for 20 min to prereact. *N*₃-TEG-NH₂ (741 μ L, 5.1 mmol, Lumiprobe) was added and the reaction stirred at room temperature for 90 min. The reaction mixture was diluted with ethyl acetate (300 mL), washed with water (3 × 100 mL), dried over magnesium sulfate, and concentrated by rotary evaporation. Product (denoted *o*NB) was purified by silica flash chromatography, 2:1 ethyl acetate:hexanes; collected the last yellow band. Yield: 849 mg, 30%. Overall yield: 18% ¹H NMR: (CDCl₃, 300 MHz) δ 7.55 (s, 1H), 7.00 (s, 1H), 6.45 (q, 1H, *J* = 6.35), 6.27 (brd t, 1H), 4.07 (t, 2H, *J* = 5.43), 3.95 (s, 3H), 3.66 (t, 2H, *J* = 4.92), 3.62 (s, 4H), 3.54 (t, 2H, *J* = 5.09), 3.44 (p, 2H, *J* = 5.22), 3.37 (t, 2H, *J* = 4.86), 3.31 (t, 2H, *J* = 6.63), 2.47–2.37 (m, 4H), 2.17 (t, 2H, *J* = 6.69), 1.87 (q, 2H, *J* = 9.15), 1.60 (d, 3H, *J* = 6.39). Expected Mass: [H] 567.25, observed 567.21.

PEG-tetraBCN. Following previously published protocol⁴³, PEG-tetraamine (M_n~20 kDa, 4-arm, 1.13 g, 0.0571 mmol, JenKem Technology USA) and BCN-OSU (100 mg, 0.343 mmol, Sigma Aldrich) were added to a flame-dried scintillation vial under nitrogen. Anhydrous DMF (5 mL) and DIEA (159 μ L, 4x) was added and the reaction was stirred under nitrogen overnight at room temperature. Water (50 mL) was added to the reaction mixture which was then dialyzed in Spectrapor dialysis tubing (3k MWCO) overnight at 4 °C. The PEG-tetraBCN was recovered as a powder by lyophilization and resuspended at 10 mM in sterile-filtered PBS for gel formation.

Quantum yield determination

The quantum yield of photocleavage was determined via kinetic analysis of the cleavage reaction as observed by UV-Vis spectrometry⁵⁴. In brief, the absorbance at a given wavelength for each crosslinker (550 nm for Ru(biq)₂, 445 nm for Ru(bpy)₂, and 375 nm for *o*NB) was tracked as each sample was exposed to light. The data were fit to an equation of the form:

$$y = A_1 e^{-x/\tau_1} + A_2 e^{-x/\tau_2} + y_0 \quad (1)$$

with two time constants τ_1 and τ_2 that give rate constants k_1 and k_2 according to

$$k_1 = -\frac{1}{\tau_1}, k_2 = -\frac{1}{\tau_2} \quad (2)$$

The quantum yield (Φ) was extracted from the rate constant for each crosslinker according to

$$\Phi = \frac{k_1 [A]_i V_{sample}}{\frac{P}{E_{ph} N_A}} \quad (3)$$

Where:

k_1 is the rate constant for photolysis

[A]_i is the initial concentration of the crosslinker

V_{sample} is the total volume of the sample irradiated

P is the power of the incoming light, measured in Watts (J sec⁻¹)

E_{ph} is the energy of the photon, given by $\frac{hc}{\lambda}$, where h is Plank's constant, c is the speed of light in a vacuum, and λ is the wavelength of incident light

N_A is Avogadro's number

Hydrogel formation

Stock solutions of Rubiq and Rubpy crosslinkers were created at 40 mM in PBS and stored at -80 °C until use. Stock solutions of *o*NB were made at 200 mM in DMSO and stored at -80 °C until use. Hydrogels were formed via SPAAC by mixing PEG-tetraBCN (final concentration of 3 mM) with the diazide crosslinkers (final concentration of 6 mM) with PBS as additional buffer. For hydrogels used in cell culture, an azide-modified RGD peptide (*N*₃-GRGDSG-NH₂) was included (final concentration of 1 mM) and cell media was used in place of PBS.

Rheometric characterization of hydrogel viscoelasticity

Hydrogels were formed on the rheometer (20 μ L, working distance = 0.3 mm) and gelation was observed in a timesweep experiment (angular frequency = 6.28 rad s⁻¹). Following complete hydrogel formation as indicated by storage modulus plateau, gels were swelled in 0.1 mM NaN₃ to cap any remaining BCN groups prior to photo-degradation. Hydrogels were exposed to light via a quartz bottom plate coupled to a fiber optic light guide from a multiwavelength LED light source.

Ex vivo degradation through pork belly tissue

Hydrogels were placed in between layers of pork belly purchased from a local butcher (B & E Meats and Seafood, Seattle, WA). For the duration of the experiment, the pork belly and light source was kept in a dark room and covered with moist paper towels to prevent drying. A multiwavelength LED light source was placed directly on the skin and tuned to the maximum power for each wavelength: 617 nm: 350 mW cm⁻², 530 nm: 314 mW cm⁻², 405 nm: 662 mW cm⁻².

Mammalian cell culture

All cells were grown to 90% confluence at 37 °C and 5% CO₂ before use for experiments. 10T1/2 fibroblast-like cells isolated from mouse embryo cells were gifted by Dr. Jennifer Davis (University of Washington). Mouse 10T1/2 fibroblasts were cultured in DMEM with 100 mM penicillin and streptomycin (p/s) and 10% fetal bovine serum (FBS). Fluorescent and non-fluorescent hSS human stromal cells (from a White, 30-year-old, male) were gifted by Dr. Beverly Torok-Storb (Fred Hutch) (originally purchased from ATCC). hSSs were cultured in RPMI media with 100 mM p/s and 10% FBS. Human bone-marrow derived mesenchymal stem cells (hMSCs) were purchased from Sigma Aldrich. hMSCs were cultured in DMEM (100 mM p/s, 10% FBS) to confluence following thawing and then in MesenPRO medium (Gibco) following the first passage.

Cell viability following exposure to Rubiq and Rubpy crosslinkers

hSS and 10T1/2 cells were plated at 1500 cells per well in a white-walled 96-well plate. 24 h after plating, cells were exposed to Rubiq, Rubpy, or Rubiq/Rubpy prereacted with monofunctionalized methoxy-PEG-BCN (M_n~10 kDa) at a final concentration of 1 mM in the appropriate growth media for 1 h. The media was then replaced with fresh media supplemented with substrate and nLuc enzyme for RealTime Glo assay (Promega). Luminescence was observed over the course of 72 h by plate reader, with an increase in luminescence suggesting an increase in cell proliferation.

Cell encapsulation in PEG hydrogels

Trypsinized cells (i.e., 10T1/2s, hSSs, hMSCs) were each encapsulated in SPAAC hydrogels at 5 × 10⁶ cells mL⁻¹ via direct mixing with hydrogel

precursors. Hydrogels (10 μ L) were formed and incubated at 37 °C and 5% CO₂ for 30 min before being submerged in the appropriate media (see Mammalian Cell Culture section).

Encapsulated cell viability

Encapsulated cell viability was assayed by live/dead staining with calcein green and ethidium homodimer (EtHD), respectively. Hydrogels were washed in PBS and incubated in live/dead staining solution (4 μ M EtHD, 2 μ M calcein) for 1 h prior to confocal imaging. Live/dead cell count was quantified from max intensity projections spanning 40 μ m \times 50 μ m \times 50 μ m of hydrogel using CellProfiler and normalized to cell viability in TEG-crosslinked hydrogels.

Released cell viability

Viability of released cells were assessed via flow cytometry. Cell-laden hydrogels were degraded using the appropriate wavelength of light (10 mW cm⁻²) into 1 mL sterile PBS. Cells were collected by pelleting and resuspended in calcein/EtHD solution for 15 min before storing on ice and FACS counting.

EdU assay for cell proliferation

Cell-laden hydrogels were cast in glass-bottom 35 mm petri dishes. 24 h after casting, hydrogels were degraded with the appropriate wavelength of light (10 mW cm⁻² for all wavelengths) into a minimum of PBS (200–300 μ L). Cells were allowed to attach to the surface for 2 h before the appropriate growth media supplemented with 10 μ M EdU was added. After 72 h cells were fixed, permeabilized, and new DNA with incorporated EdU was tagged with AF-568-azide (Lumiprobe) via copper-catalyzed azide-alkyne cycloaddition (ClickIT EdU assay, Invitrogen). Nuclei were stained with Hoescht and fluorescently imaged. CellProfiler was used to count the total number of nuclei and number of EdU⁺ nuclei.

Caspase 3 assay for apoptosis

hSS and 10T1/2 cells were plated at 1500 cells per well in a white-walled 96-well plate. 24 h after plating, cells were exposed to Rubiq, Rubpy, or Rubiq/Rubpy prereacted with mono-PEG-BCN at a final concentration of 1 mM in the appropriate growth media for 3 h. 24 h after exposure, caspase 3 levels were determined via the ApoTox Glo assay, where an increase in luminescence indicates increased levels of caspase 3 and the presence of apoptotic cells (Promega).

Photorelease of human stromal cells from gels for flow cytometry

hSS stromal cells stably expressing BFP, GFP, and mCherry were encapsulated in PEG-tetraBCN hydrogels crosslinked with the appropriate photocleavable crosslinker (Rubiq with hSS-mCherry⁺, Rubpy with hSS-GFP⁺, and oNB with hSS-BFP⁺). All three hydrogels were cast in the same tissue culture dish, allowed to form for 30 min, then incubated in RPMI media for 24 h.

Hydrogels were transferred to PBS and exposed to 617 nm, 530 nm, or 405 nm light (10 mW cm⁻², until hydrogel degradation was observed) and the resulting cell suspension was collected and analyzed by flow cytometry. Any hydrogels left intact after irradiation were imaged using confocal fluorescent microscopy.

Statistics & reproducibility

Unless indicated otherwise, all experiments were performed with $N = 3$ replicates (3 biological replicates). No statistical method was used to predetermine sample size. No data were excluded from the analyses.

Reporting summary

Further information on research design is available in the Nature Portfolio Reporting Summary linked to this article.

Data availability

All data supporting the findings of this study are available within the article and its supplementary files. Any additional requests for information can be directed to, and will be fulfilled by, the lead contact. Source data are provided with this paper.

References

1. Ruskowitz, E. R. & DeForest, C. A. Photoresponsive biomaterials for targeted drug delivery and 4D cell culture. *Nat. Rev. Mater.* **3**, 17087 (2018).
2. Rapp, T. L. & DeForest, C. A. Visible Light-Responsive Dynamic Biomaterials: Going Deeper and Triggering More. *Adv. Healthc. Mater.* **9**, 1901553 (2020).
3. Rapp, T. L. & DeForest, C. A. Targeting drug delivery with light: A highly focused approach. *Adv. Drug Deliv. Rev.* **171**, 94–107 (2021).
4. Munoz-Robles, B. G., Kopyeva, I. & DeForest, C. A. Biomaterials: Surface Patterning of Hydrogel Biomaterials to Probe and Direct Cell-Matrix Interactions (Adv. Mater. Interfaces 21/2020). *Adv. Mater. Interf.* **7**, 2070116 (2020).
5. Gilbert, P. M. et al. Substrate elasticity regulates skeletal muscle stem cell self-renewal in culture. *Science* **329**, 1078–1081 (2010).
6. Hofer, M. & Lutolf, M. P. Engineering organoids. *Nat. Rev. Mater.* **6**, 402–420 (2021).
7. Tibbitt, M. W. & Anseth, K. S. Hydrogels as extracellular matrix mimics for 3D cell culture. *Biotechnol. Bioeng.* **103**, 655–663 (2009).
8. Yang, C., Tibbitt, M. W., Basta, L. & Anseth, K. S. Mechanical memory and dosing influence stem cell fate. *Nat. Mater.* **13**, 645–652 (2014).
9. Elosegui-Artola, A., et al. Matrix viscoelasticity controls spatio-temporal tissue organization. *Nat. Mater.* **22**, 117–127 (2023).
10. Below, C. R. et al. A microenvironment-inspired synthetic three-dimensional model for pancreatic ductal adenocarcinoma organoids. *Nat. Mater.* **21**, 110–119 (2021).
11. Fang, Y. & Eglen, R. M. Three-Dimensional Cell Cultures in Drug Discovery and Development. *SLAS Discov.* **22**, 456–472 (2017).
12. Antonica, F. et al. Generation of functional thyroid from embryonic stem cells. *Nature* **491**, 66–71 (2012).
13. Huch, M. et al. In vitro expansion of single Lgr5+ liver stem cells induced by Wnt-driven regeneration. *Nature* **494**, 247–250 (2013).
14. Lancaster, M. A. et al. Cerebral organoids model human brain development and microcephaly. *Nature* **501**, 373–379 (2013).
15. Mateen, R., Ali, M. M. & Hoare, T. A printable hydrogel microarray for drug screening avoids false positives associated with promiscuous aggregating inhibitors. *Nat. Commun.* **9**, 602 (2018).
16. DeForest, C. A. & Tirrell, D. A. A photoreversible protein-patterning approach for guiding stem cell fate in three-dimensional gels. *Nat. Mater.* **14**, 523–531 (2015).
17. Kirschner, C. M., Alge, D. L., Gould, S. T. & Anseth, K. S. Clickable, photodegradable hydrogels to dynamically modulate valvular interstitial cell phenotype. *Adv. Healthc. Mater.* **3**, 649–657 (2014).
18. Gjorevski, N., et al. Tissue geometry drives deterministic organoid patterning. *Science* **375**, eaaw9021 (2022).
19. Yavitt, F. M., Kirkpatrick, B. E., Blatchley, M. R. & Anseth, K. S. 4D Materials with Photoadaptable Properties Instruct and Enhance Intestinal Organoid Development. *ACS Biomater. Sci. Eng.* <https://doi.org/10.1021/acsbiomaterials.1c01450> (2022).
20. Killaars, A. R. et al. Extended Exposure to Stiff Microenvironments Leads to Persistent Chromatin Remodeling in Human Mesenchymal Stem Cells. *Adv. Sci.* **6**, 1801483 (2019).
21. Walker, C. J. et al. Nuclear mechanosensing drives chromatin remodelling in persistently activated fibroblasts. *Nat. Biomed. Eng.* **5**, 1485–1499 (2021).

22. Shadish, J. A., Benuska, G. M. & DeForest, C. A. Bioactive site-specifically modified proteins for 4D patterning of gel biomaterials. *Nat. Mater.* **18**, 1005–1014 (2019).

23. Batalov, I., Stevens, K. R. & DeForest, C. A. Photopatterned biomolecule immobilization to guide three-dimensional cell fate in natural protein-based hydrogels. *Proc. Natl. Acad. Sci. USA* **118**, e2014194118 (2021).

24. Cai, Z. et al. Precise Construction of Cell-Instructive 3D Micro-environments by Photopatterning a Biodegradable Hydrogel. *Chem. Mater.* **31**, 4710–4719 (2019).

25. Headen, D. M. et al. Local immunomodulation with Fas ligand-engineered biomaterials achieves allogeneic islet graft acceptance. *Nat. Mater.* **17**, 732–739 (2018).

26. Azagarsamy, M. A., McKinnon, D. D., Alge, D. L. & Anseth, K. S. Coumarin-Based Photodegradable Hydrogel: Design, Synthesis, Gelation, and Degradation Kinetics. *ACS Macro. Lett.* **3**, 515–519 (2014).

27. Azagarsamy, M. A. & Anseth, K. S. Wavelength-controlled photocleavage for the orthogonal and sequential release of multiple proteins. *Angew. Chemie - Int. Ed.* **52**, 13803–13807 (2013).

28. Pelloth, J. L., et al Wavelength-Selective Softening of Hydrogel Networks. *Adv. Mater.* **2102184** <https://doi.org/10.1002/ADMA.202102184> (2021).

29. Jacques, S. L. Optical properties of biological tissues: A review. *Phys. Med. Biol.* **58**, R37–R61 (2013).

30. Rapp, T. L., Wang, Y., Delessio, M. A., Gau, M. R. & Dmochowski, I. J. Designing photolabile ruthenium polypyridyl crosslinkers for hydrogel formation and multiplexed, visible-light degradation. *RSC Adv.* **9**, 4942–4947 (2019).

31. Griffin, D. R. & Kasko, A. M. Photodegradable macromers and hydrogels for live cell encapsulation and release. *J. Am. Chem. Soc.* **134**, 13103–13107 (2012).

32. Menzel, J. P. et al. Light-Controlled Orthogonal Covalent Bond Formation at Two Different Wavelengths. *Angew. Chemie Int. Ed.* **58**, 7470–7474 (2019).

33. Truong, V. X., Bachmann, J., Unterreiner, A., Blinco, J. P. & Barner-Kowollik, C. Wavelength-Orthogonal Stiffening of Hydrogel Networks with Visible Light. *Angew. Chemie Int. Ed.* **61**, e202113076 (2022).

34. Zayat, L., Calero, C., Alborés, P., Baraldo, L. & Etchenique, R. A new strategy for neurochemical photodelivery: metal-ligand heterolytic cleavage. *J. Am. Chem. Soc.* **125**, 882–883 (2003).

35. Li, A., Turro, C. & Kodanko, J. J. Ru(II) polypyridyl complexes as photocages for bioactive compounds containing nitriles and aromatic heterocycles. *Chem. Commun.* **54**, 1280–1290 (2018).

36. Griepenburg, J. C., Rapp, T. L., Carroll, P. J., Eberwine, J. & Dmochowski, I. J. Ruthenium-caged antisense morpholinos for regulating gene expression in zebrafish embryos. *Chem. Sci.* **6**, 2342–2346 (2015).

37. Rapp, T. L., Highley, C. B., Manor, B. C., Burdick, J. A. & Dmochowski, I. J. Ruthenium-Crosslinked Hydrogels with Rapid, Visible-Light Degradation. *Chem. - A Eur. J.* **24**, 2328–2333 (2018).

38. Arora, K. et al. Catch and Release Photosensitizers: Combining Dual-Action Ruthenium Complexes with Protease Inactivation for Targeting Invasive Cancers. *J. Am. Chem. Soc.* **140**, 14367–14380 (2018).

39. Havrylyuk, D., Hachey, A. C., Fenton, A., Heidary, D. K. & Glazer, E. C. Ru(II) photocages enable precise control over enzyme activity with red light. *Nat. Commun.* **13**, 3636 (2022).

40. Sun, W. et al. An Amphiphilic Ruthenium Polymetallodrug for Combined Photodynamic Therapy and Photochemotherapy In Vivo. *Adv. Mater.* **29**, 1603702 (2017).

41. Al-Afyouni, M. H., Rohrbaugh, T. N., Al-Afyouni, K. F. & Turro, C. New Ru(II) photocages operative with near-IR light: new platform for drug delivery in the PDT window. *Chem. Sci.* **9**, 6711–6720 (2018).

42. Havrylyuk, D., Stevens, K., Parkin, S. & Glazer, E. C. Toward Optimal Ru(II) Photocages: Balancing Photochemistry, Stability, and Biocompatibility Through Fine Tuning of Steric, Electronic, and Physicochemical Features. *Inorg. Chem.* **59**, 1006–1013 (2020).

43. Badeau, B. A., Comerford, M. P., Arakawa, C. K., Shadish, J. A. & DeForest, C. A. Engineered modular biomaterial logic gates for environmentally triggered therapeutic delivery. *Nat. Chem.* **10**, 251–258 (2018).

44. Agard, N. J., Prescher, J. A. & Bertozzi, C. R. A strain-promoted [3 + 2] azide-alkyne cycloaddition for covalent modification of biomolecules in living systems. *J. Am. Chem. Soc.* **126**, 15046–15047 (2004).

45. Dixon, I. M., Bonnet, S., Alary, F. & Cuny, J. Photoinduced Ligand Exchange Dynamics of a Polypyridyl Ruthenium Complex in Aqueous Solution. *J. Phys. Chem. Lett.* **12**, 7278–7284 (2021).

46. Loftus, M., Al-Afyouni, D. & Turro, C. New Ru II Scaffold for Photo-induced Ligand Release with Red Light in the Photodynamic Therapy (PDT) Window. *Chem. Eur. J.* **24**, 11550–11553 (2018).

47. Demas, J. N., Diemente, J. & Harris, E. W. Oxygen Quenching of Charge-Transfer Excited States of Ruthenium (II) Complexes. Evidence for Singlet Oxygen Production. *J. Am. Chem. Soc.* **95**, 6864–6865 (1973).

48. Papish, E. T. & Oladipupo, O. E. Factors that influence singlet oxygen formation vs. ligand substitution for light-activated ruthenium anticancer compounds. *Curr. Opin. Chem. Biol.* **68**, 102143 (2022).

49. White, J. K., Schmehl, R. H. & Turro, C. An overview of photo-substitution reactions of Ru(II) imine complexes and their application in photobiology and photodynamic therapy. *Inorganica Chimica Acta.* **454**, 7–20 (2017).

50. Lee, U. N. et al. Layer-by-layer fabrication of 3D hydrogel structures using open microfluidics. *Lab Chip* **20**, 525–536 (2020).

51. Askes, S. H. C., Meijer, M. S., Bouwens, T., Landman, I. & Bonnet, S. Red Light Activation of Ru(II) Polypyridyl Prodrugs via Triplet-Triplet Annihilation Upconversion: Feasibility in Air and through Meat. *Mol.* **21**, 1460 (2016).

52. DeForest, C. A., Polizzotti, B. D. & Anseth, K. S. Sequential click reactions for synthesizing and patterning three-dimensional cell microenvironments. *Nat Mater.* **8**, 659–664 (2009).

53. Wachter, E., Heidary, D. K., Howerton, B. S., Parkin, S. & Glazer, E. C. Light-activated ruthenium complexes photobind DNA and are cytotoxic in the photodynamic therapy window. *Chem. Commun.* **48**, 9649–9651 (2012).

54. Rapp, T. L., Phillips, S. R. & Dmochowski, I. J. Kinetics and Photochemistry of Ruthenium Bisbipyridine Diacetonitrile Complexes: An Interdisciplinary Inorganic and Physical Chemistry Laboratory Exercise. *J. Chem. Educ.* **93**, 2101–2105 (2016).

Acknowledgements

The authors would like to acknowledge R. Bretherton and I. Kopyeva for helpful suggestions related to cell culture. This work was supported by a CAREER Award (DMR 1652141, C.A.D.) and grants (DMR 1807398, C.A.D.) from the National Science Foundation, as well as a Maximizing Investigators' Research Award (R35GM138036, C.A.D.) from the National Institutes of Health. Postdoctoral fellowship support was provided by the Washington Research Foundation (to T.L.R.). Part of this work was conducted with instrumentation provided by the Joint Center for Deployment and Research in Earth Abundant Materials (JCDREAM).

Author contributions

For this manuscript, T.L.R. and C.A.D. conceived and designed the experiments; T.L.R. performed the experiments and analyzed the data; T.L.R. and C.A.D. prepared the figures; T.L.R. and C.A.D. wrote the paper.

Competing interests

The authors declare no competing interests.

Additional information

Supplementary information The online version contains supplementary material available at
<https://doi.org/10.1038/s41467-023-40805-w>.

Correspondence and requests for materials should be addressed to Cole A. DeForest.

Peer review information *Nature Communications* thanks Edith Glazer, and the other, anonymous, reviewer(s) for their contribution to the peer review of this work.

Reprints and permissions information is available at
<http://www.nature.com/reprints>

Publisher's note Springer Nature remains neutral with regard to jurisdictional claims in published maps and institutional affiliations.

Open Access This article is licensed under a Creative Commons Attribution 4.0 International License, which permits use, sharing, adaptation, distribution and reproduction in any medium or format, as long as you give appropriate credit to the original author(s) and the source, provide a link to the Creative Commons licence, and indicate if changes were made. The images or other third party material in this article are included in the article's Creative Commons licence, unless indicated otherwise in a credit line to the material. If material is not included in the article's Creative Commons licence and your intended use is not permitted by statutory regulation or exceeds the permitted use, you will need to obtain permission directly from the copyright holder. To view a copy of this licence, visit <http://creativecommons.org/licenses/by/4.0/>.

© The Author(s) 2023